A Novel Ti_{12}-based Metal-Organic Framework for Photocatalytic Hydrogen Evolution

Bingbing CHEN[1], Asma MANSOURI[1], Celia M. RUEDA-NAVARRO[2], Iurii DOVGALIUK[1], Philippe BOULLAY[3], Gilles PATRIARCHE[4], Beibei XIAO[5,6], Dong FAN[5], Arianna MELILLO[1], Lokuge Aravindani FERNANDO,[1] Guillaume MAURIN[5], Sergio NAVALÓN[2], Hermenegildo GARCIA[2], Georges MOUCHAHAM*[1] and Christian SERRE*[1]

1, Institut des Matériaux Poreux de Paris, Ecole Normale Supérieure, ESPCI Paris, CNRS, PSL University, 75005 Paris, France; Emails : georges.mouchaham@ens.psl.eu ; christian.serre@ens.psl.eu.

2, Departamento de Química, Universitat Politècnica de València, C/Camino de Vera, s/n, 46022 Valencia, Spain.

3, CRISMAT, CNRS, Normandie Univ., ENSICAEN, UNICAEN, 14000 Caen, France

4, Centre de Nanosciences et de Nanotechnologies, CNRS, Université Paris Saclay, Palaiseau, France.

5, ICGM, Univ. Montpellier, CNRS, ENSCM, Montpellier, France.

6, School of Energy and Power Engineering, Jiangsu University of Science and Technology, Zhenjiang, Jiangsu, 212003, China.

Abstract

Constructing titanium-based metal-organic frameworks (Ti-MOFs) is an effective way towards upgrading TiOx and the enhancement of their photocatalytic performance throughout higher accessibility to active sites and better tunability of photophysical properties. In this regard, Ti-MOFs have attracted much attention as photocatalyst candidates owing to their porosity and tunability in terms of chemical composition and pore engineering. However, Ti-MOFs remain still one of the least developed sub-class of MOF materials because of the complexity of titanium chemistry in solution hampering their rational design, despite recent progresses. Here, we present a new microporous Ti-MOFs with *acs* topology, labeled MIP-209(Ti) (MIP stands for Materials from Institute of Porous Materials of Paris) constructed by a nitro terephthalate ligand and $Ti_{12}O_{15}$ oxo-clusters, as revealed by continuous rotation electron diffraction (cRED). MIP-209(Ti) can be obtained using various terephthalate (1,4-BDC^{2-}) derivatives such as NO_2-BDC and 2Cl-BDC using an eco-friendly solvent, suggesting the ability of Ti_{12}-MOFs for isostructural chemistry. Alternatively, it is also possible to tune the composition of its Ti-oxo-cluster, similarly to MIP-177(Ti)-LT bearing the same $Ti_{12}O_{15}$ sub-unit. Typically, low percentage Cr^{3+} doping (≤ 5 at%) in MIP-209(Ti) favorably enhances the water stability. Interestingly, photocatalytic hydrogen evolution from water splitting reaction (HER) were measured for MIP-209(Ti-Cr)-NO_2 and a significant hydrogen production rate, with good reusability and stability under simulated solar light irradiation, were revealed. It showed enhanced photocatalytic hydrogen production performances under simulated solar light irradiation compared to the benchmark Ti-MOF IEF-11 with a fourfold enhanced hydrogen production in HER in 5h in presence of methanol (5812 µmol of H_2/g_{cat} against 1391 µmol of H_2/g_{cat}) as well as, without any noble metal co-catalyst, a 6-fold enhanced overall water splitting production (681 and 325 µmol/g_{cat} of H_2 and O_2, respectively for MIP-209, against 94 and 53 µmol/g_{cat} of H_2 and O_2, respectively, for IEF-11). This work represents a leap forward in the synthesis of Ti-MOFs and their practical photocatalytic applications.

Introduction

Titanium dioxide (TiO_2) has demonstrated great potential as an inorganic semiconducting photocatalyst owing to its environmentally friendly, earth-abundant and remarkable stable properties.[1,2] However, the enhancement of its photocatalytic performance is still strongly desired via introduction of visible light photoresponse, enhancement of reactant adsorption capacity, and simplification of separation from the suspension.[3-6] Compared with TiO_2 nanoparticles, long-range order Ti-O oxo-clusters in titanium-based MOFs (Ti-MOFs), can promote enhanced accessibility to active sites, where the Ti-oxo-cluster can be assimilated as molecular TiOx with significantly higher accessible surface area, while the porosity of the framework can ensure the diffusion of reactants and products. Besides, the hybrid (organic-inorganic) nature of MOFs is a key feature to tune the photophysical properties and to expand the photocatalytic reaction to the visible range via the rational design of organic moieties and inorganic building units.[7-10] If early works have been reported only Ti phosphonate based MOFs with a limited porosity,[11-13] since 2009, highly porous crystalline titanium-carboxylate-based MOFs (Ti-MOFs) built by the assembly of various organic linkers and titanium-based inorganic building units have emerged and their properties have been assessed for diverse photocatalytic reactions such as hydrogen evolution reaction (HER),[14-18] overall water splitting (OWS) into H_2 and O_2 in a stoichiometric amount,[19-23] CO_2 reduction,[24] and pollutant degradation among others.[25,26] Nevertheless, there is still only scarce examples reported on Ti-MOFs as photocatalysts for HER or OWS under visible light or sunlight irradiation.[15-17,22,24] Meanwhile, the rational design of new porous crystalline Ti-MOFs remains still elusive mainly due to the poor control of the chemistry of titanium in solution.[7] For instance, while more than 100,000 different MOF structures have been reported so far, less than 40 Ti-MOFs structures obtained via one-step synthesis and bimetallic Ti-MOFs have been reported to date.[8,27-30] Several challenges on Ti-MOFs stem from the synthesis procedure, the structural determination and sometimes their chemical stability especially under practical photocatalytic test conditions.

The use of air-stable or hydrophobic Ti precursors, e.g., $Ti(iPrO)_4$, $TiOSO_4$, $TiO(acac)_2$ (acac: acetylacetonate) even pre-formed Ti-oxo-clusters, is in most cases required to avoid uncontrolled titanium hydrolysis during the Ti-MOFs synthesis.[31,32] Additionally, several attempts to reach a more rational approach have been recently proposed such as using inhibitors to better control the trade-off of M-O bond association and dissociation rate.[7] However, the synthesis methods of Ti-MOFs are still driven by serendipity as evidenced by the large diversity of inorganic building units (IBU) that

range from discrete Ti octahedra to infinite Ti-oxo-chains, with almost a different IBU per type of ligand.[7] Recently, several new Ti-MOFs were obtained under acidic conditions which offers new opportunities to extend the Ti-MOF library.[33-35] In comparison with the more discrete IBUs generally obtained when using pure organic solvents (DMF, alcohols), it appears that higher nuclearity IBUs ($Ti_{12}O_{15}$ and $Zr_{12}O_8(OH)_{14}$) oxo-clusters have been attained under pure acid solvothermal conditions (formic or acetic acids) leading to the highly porous robust MIP-177(Ti)-LT and MIP-206(Zr) frameworks, respectively.[33,36] Interestingly, when using less acidic polar solvents such as isopropanol (in presence of imidazole),[18] one could also obtain MOFs based on 1-D Ti-oxide nanorods such as ICGM-1, a polymorph to MIL-125(Ti)-NH_2 and the ZSTU series built up from tricarboxylate linkers.[37] Moreover, starting from the same topology and integrating different functional or extended ligands can lead to an isostructural platform of Ti-MOFs that might provide a rational way to tune their physical/chemical properties, such as porosity, hydrophilicity, bandgap, etc.[38] Till now, such an approach was successfully applied on a very limited number of Ti-MOFs (MIL-125(Ti)-NH_2,[39] ZSTU-1/2/3,[15] UCFMOF-1/2/3/4,[40] MOF-901/2[41]) prepared via a direct synthesis route. Another possibility is to rely on the multivariate approach to tune the properties of a given MOF (MTV-MOFs), in order to endow the pores with a new level of complexity to fine-tune the pore environment and resulting properties.[36,42] Recently this strategy has been applied for several Ti-MOFs such as PCN-415,[29] MUV-10,[43] MIP-208,[35] and cMUV-11[44] leading to enhance their porosity and their performance for CO_2/N_2 separation and CO_2 photo-methanation.

The second key challenge of Ti-MOFs' development lies in their crystal structure determination. Very often, poorly crystalline samples are obtained, precluding from their *ab initio* structure determination. To date only a few Ti-MOFs structures e.g., DGIST-1,[45] cMUV-11[44] and PCN-22[46], have been solved from single crystal data. In general, only powders are obtained (e.g., MIP-177(Ti)-LT/HT,[33] ACM-1,[47] ICGM-1[18]) requiring the use of high resolution powder X-ray diffraction (PXRD), combining direct structure solution (e.g., charge flipping) and refinement (the Rietveld method), and in most cases complemented by density functional theory (DFT) calculations. The use of electron diffraction (ED) is equally required to enable rapid data collection time (minutes or less), low dose measurement and high accuracy by integrating reflection intensity.[48-50] MOF crystals should, however, be slightly resistant to electron beam exposure and in the case of Ti-MOFs, this was successfully applied for instance with COK-47[51] and IEF-11[22].

Herein, we present a new microporous Ti-MOF with *acs* topology, labeled MIP-209(Ti), constructed from a nitro terephthalate derivative ligand and $Ti_{12}O_{15}$ clusters with the

general formula $Ti_{12}O_{15}(NO_2\text{-}1,4\text{-}BDC)_6(acetate)_3$. As revealed by continuous rotation electron diffraction (cRED), the structure of MIP-209(Ti)-NO_2 crystalizes in a hexagonal space group $P6_3/mmc$ (No. 194) with unit cell parameters of a = 22.39(6) Å and c = 16.59(5) Å. MIP-209(Ti) is obtained in solvothermal conditions (150 °C for 30 h) with the use of pure acetic acid. Additionally, it was also possible to tune the composition of its Ti_{12} oxo-cluster, similarly to MIP-177(Ti)-LT, to reach higher chemical stability. More specifically, substitution of Ti^{4+} by a low percentage of Cr^{3+} can favorably enhance the water stability, while crystallinity and porosity are maintained after soaking the solid in water for at least 7 days. Given the enhanced water stability and the intrinsic photophysical properties of MIP-209(Ti-Cr)-NO_2, its photocatalytic HER and OWS activities were evaluated under simulated sunlight irradiation. MIP-209(Ti-Cr)-NO_2 displayed a substantially high hydrogen production rate with good reusability and stability in presence of methanol as scavenger under simulated sunlight irradiation, achieving a fourfold (5812 µmol of H_2/g_{cat} in 5 h) enhanced hydrogen production, compared with the benchmark MOF IEF-11 (1391 µmol of H_2/g_{cat} in 5 h).[22] Besides that, the noble metal-free MIP-209(Ti-Cr)-NO_2 showed 6-fold enhanced hydrogen production (681 µmol of H_2/g_{cat} in 5 h) in OWS reaction under simulated solar light irradiation, in comparison with the best Ti-MOF reported so far for this reaction, i.e., IEF-11 (94 µmol of H_2/g_{cat} in 5 h).

Results

Synthesis and structure solution

MIP-209(Ti)-NO_2 was prepared through a one-step green solvothermal reaction by mixing titanium (IV) isopropoxide and 2-nitro-terephthalic acid in acetic acid. The mixture was heated at 150 °C for ca. 30 h before being filtered at room temperature. The solid was then washed in warm (60 °C) ethanol, filtered and air-dried to yield MIP-209(Ti)-NO_2 (0.5 g, 23% yield based on ligand) as off-white microcrystalline powder. Powder X-ray diffraction (PXRD) patterns and scanning electron microscopy (SEM) (**Figure S1 and S2**) images, showed a gradual crystallization of MIP-209(Ti)-NO_2 with optimal formation after 30 h synthesis in the described conditions. The high thermal stability of the MOF (> 300 °C) was confirmed by variable temperature PXRD and thermogravimetric analysis (TGA) in O_2 (**Figure S3 and S4**). Nitrogen porosimetry data collected at 77 K led to a Brunauer-Emmett-Teller (BET) area of 830(10) $m^2\ g^{-1}$ and a free pore volume of 0.31(7) $cm^3\ g^{-1}$ (**Figure S5**). It is to be noted that a color change, from white to yellowish, occurred when the powder was activated at 200 °C under vacuum condition (**Figure S6**). Besides, MIP-209(Ti)-NO_2 was further characterized

by Fourier transform infrared spectroscopy (FT-IR) showing that there is still residual trace of free (uncoordinated) carboxylic group from the tiny absorbance band of C=O between 1715-1750 cm^{-1} (**Figure S7**). CO_2 and H_2O sorption isotherms were also measured at 298 K. The near-linear CO_2 adsorption isotherm demonstrated relatively weak host/guest interactions, and the S-shaped water adsorption isotherm revealed that MIP-209(Ti)-NO_2 exhibits a relatively mild hydrophobic behavior which may be accounted to the methyl group of the acetate moieties (**Figure S8 and S9**).

Initial attempts to solve the structure from high resolution PXRD did not lead to a satisfying structure solution, very likely as consequence of the small size of orthogonal nanoparticles of 100-350 nm in length and 25-100 nm in width according to SEM (**Figure S1**). Thus, the local arrangement of the titanium atoms was investigated by high-energy synchrotron X-rays pair distribution function (PDF) analysis collected at the CRISTAL beamline of synchrotron SOLEIL. To make a comparison with the local organization of MIP-177(Ti)-LT, a Ti-MOF bearing the same $Ti_{12}O_{15}$ clusters and synthesized in similar acidic conditions, suitable X-ray data for PDF analysis were collected in the same conditions for both MOFs. The two functions overlapped well in the short-range distances (below 6.15 Å) (**Figure 1A and S10**), indicating that the IBU of the new Ti-MOF is indeed made of $Ti_{12}O_{15}$ oxo-clusters. Then, the structure of MIP-209(Ti)-NO_2 was tentatively solved by continuous rotation electron diffraction (cRED), one of the so-called 3D ED approaches enabling fast single-crystal ED data collection for the structure determination of electron beam sensitive materials such as MOFs.[52] Several cRED datasets were collected on isolated nanocrystals (**Figure 1B and S11**) and analyzed following a protocol detailed in Supplementary Information. Two of the best datasets were merged in order to obtain more than 90% completeness for a 1.1 Å resolution shell (**Table S1**). This proved to be sufficient for a successful *ab-initio* structure determination. From the obtained electrostatic potential map (**Figure S12**), the whole framework of MIP-209(Ti)-NO_2 can be derived with well-identified atomic positions for the $Ti_{12}O_{15}$ oxo-clusters and the nitro terephthalate ligands. The model was then further refined against the cRED data. Calculating the difference Fourier maps enables the localization of the missing nitrogen atom of the ligand NO_2 groups. For the latter, the occupancy was fixed to 1/2, indicating that the NO_2 is disordered in two opposite ortho positions on the aromatic ring (**Figure S13**). The atomic displacement parameters (ADP) of all atoms were refined isotopically. As expected for 3D ED data (due to dynamical scattering effects), the R-factors converge to high values (e.g., R(obs) = 25%) with respect to X-ray diffraction standards, but they are reasonable values for kinematically treated electron diffraction data. At this stage, some residual density in the pores was still visible in the Fourier difference map

(**Figure S13**) but difficult to interpret in the context of kinematically refined ED data. However, it could indicate the presence of residual solvent molecules (disordered molecules of water and acetic acid) well trapped within the pores during synthesis. As shown in **Figure 1C**, the structure of MIP-209(Ti)-NO_2 was validated by PXRD data refinement using the Rietveld method.[53]

Figure 2 shows that each $Ti_{12}O_{15}$ oxo-cluster in MIP-209(Ti)-NO_2 is connected to 12 carboxylate groups belonging to 12 different terephthalate linkers (grey color), arranged in pairs, bridging 6 neighboring oxo-clusters. These latter are aligned along the *c* axis (**Figure 2D**) similarly to MIP-177(Ti)-LT. However, they are arranged in a staggered mode when viewed along the orthogonal direction (**Figure 2F**), in contrast to the case of MIP-177(Ti)-LT where the oxo-clusters are in eclipsed mode along the *a* and *b* axes (**Figure 2G**). Additionally, three acetate ligands (shown in green, in **Figure 2H**) complete the remaining coordination sites on the Ti_{12}-IBU. The presence of staggered $Ti_{12}O_{15}$ oxo-clusters leads to a zig-zag shaped connectivity between adjacent oxo-clusters bridging two terephthalate ligands (**Figure S14**). Overall, this results in a 3D structure endowed with 1D nano-sized hexagonal channels running along the *c* axis and a small cage (highlighted in blue) delimited by five $Ti_{12}O_{15}$ clusters and 12 BDC-NO_2 ligands all with disordered NO_2 groups pointing towards the center of the small cage (**Figure 2D & H**). The presence of the methyl groups of the residual acetate moieties on the belt of $Ti_{12}O_{15}$ oxo-cluster results, very likely, in the relatively mild hydrophobicity of MIP-209(Ti)-NO_2 framework.

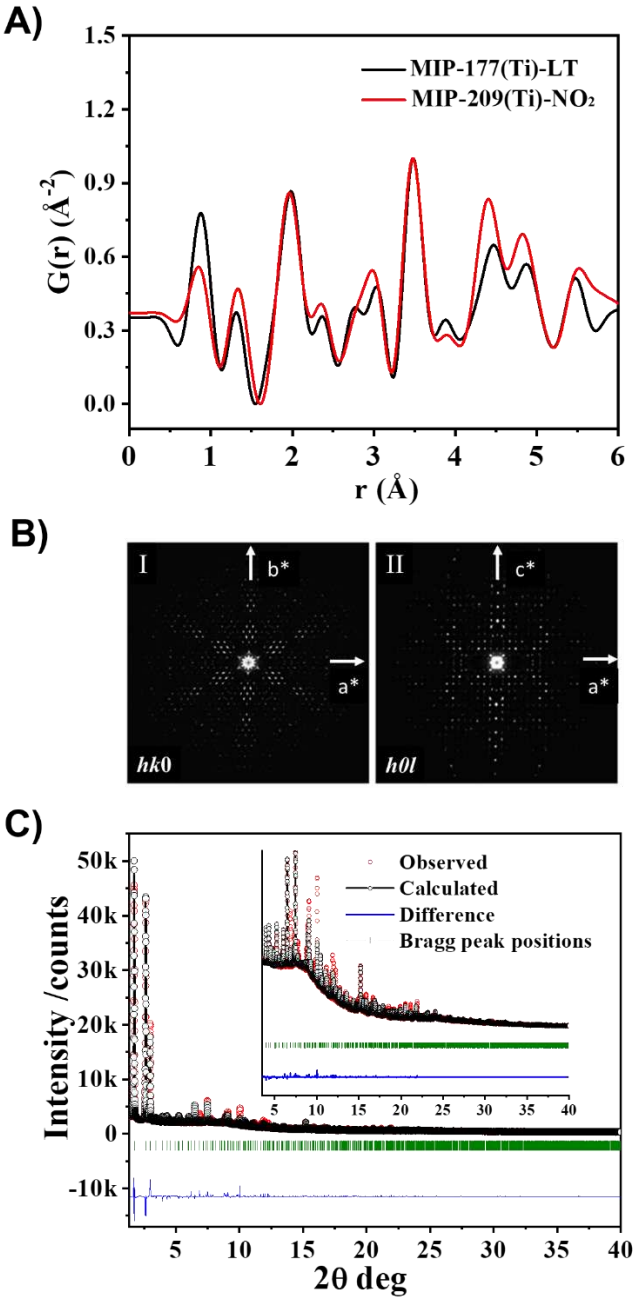

Figure 1. Structural determination of MIP-209(Ti)-NO_2. A) Synchrotron X-ray PDF data of MIP-209(Ti)-NO_2 and MIP-177(Ti)-LT. The constituents of MIP-177(Ti)-LT, $Ti_{12}O_{15}$ cluster have the maximum Ti-Ti distance (6.15 Å) in the oxo-cluster; B) symmetry averaged 2D slices of the 3D reciprocal space (I) *hk*0 and (II) *h*0*l* obtained by cRED from different datasets; C) crystal structure refinement by the Rietveld method from the laboratory high-resolution PXRD (Cu Kα1 radiation λ = 1.5406 Å).

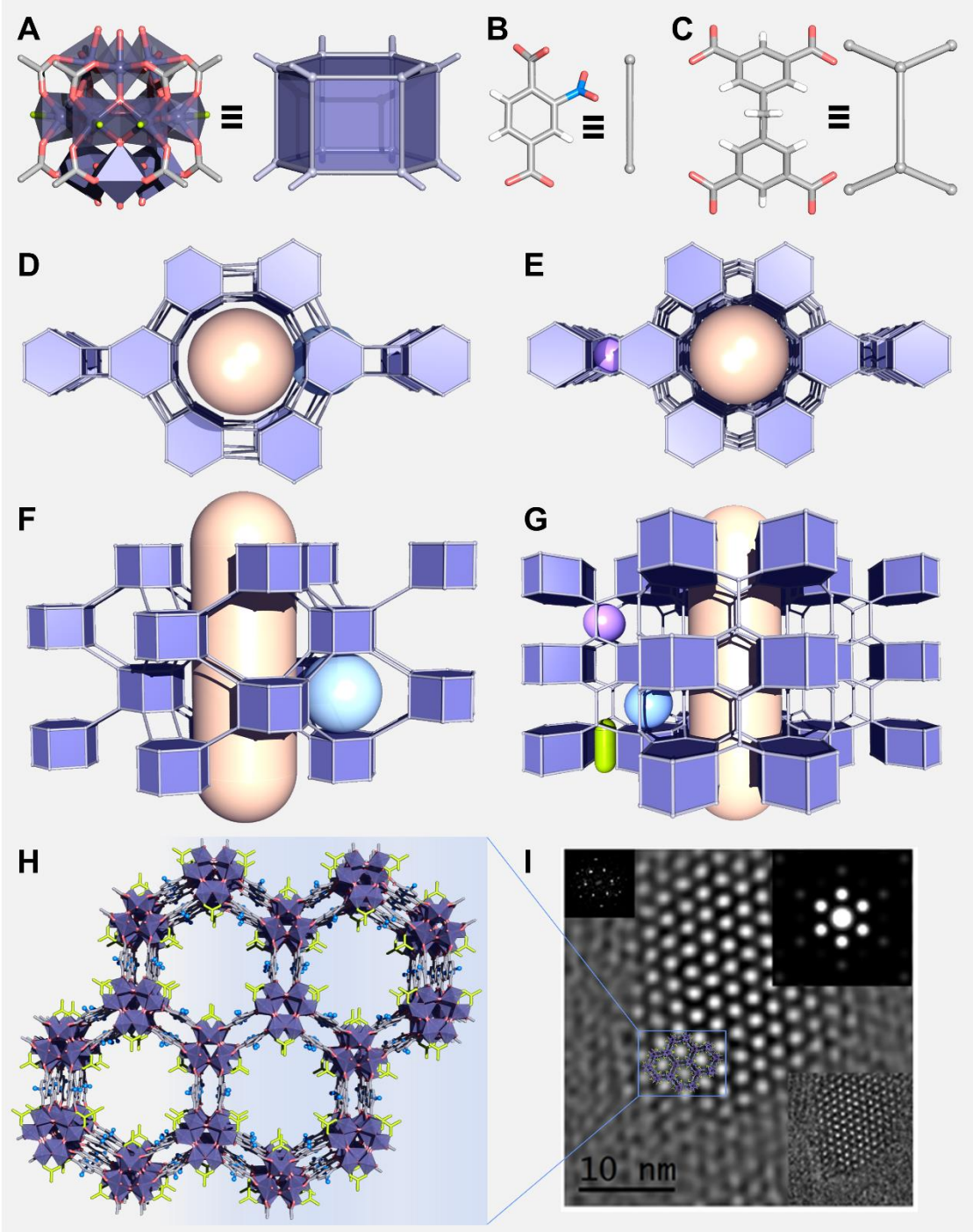

Figure 2. Crystal structure of MIP-209(Ti)-NO_2 in comparison with MIP-177(Ti)-LT. (A) the 12-connected $Ti_{12}O_{15}$ cluster and its schematic representation. (B) and (C) The organic linkers of the MIP-209(Ti)-NO_2 and the MIP-177(Ti)-LT, respectively. Views along (D) & (E) and orthogonal (F) & (G) to the hexagonal 1-D nanometric channels (illustrated in yellow rod) for MIP-209(Ti) and MIP-177(Ti)-LT, respectively, highlighting the spatial arrangement of the $Ti_{12}O_{15}$ clusters in both cases. (H) 3-D view of MIP-209(Ti)-NO_2 along the 00*l* axis. Color code: C, grey; O, red; N, blue; H, white; green, sites of non-bridging ligands (such as acetates or formates). (I) Filtered HR-TEM image of MIP-209(Ti)-NO_2 along the 00*l* axis displaying the 1-D hexagonal channels, which perfectly overlay with the crystal structure along the same direction.

Imaging the particles of the MOF using low-dose conditions was equally employed to further confirm the 3D ED model. Compared to the structural model along a certain crystallographic orientation, the high-resolution images of the surface of a particle oriented in this same orientation enable a first qualitative validation of the structure. Indeed, HR-TEM images allowed to identify the $Ti_{12}O_{15}$ oxo-clusters adopting the same zig-zag arrangements observed at the surface of a [100] axis particle (**Figure S15**). Similarly, the hexagonal-symmetry channels along the [001] axis can be observed as bright discs at the surface of a [001] axis particle (**Figure S16**). Moreover, from the several particles found along the [001] axis, visualization channel enables the measurement of their diameters using a profile line along the row of bright spots on the images (**Figure S17**). The average diameter measured is 1.1 nm, thus agreeing with the pore size distribution found from the nitrogen adsorption isotherm at 77 K as well as the values deduced from the DFT-geometry optimized structure model (**Figure S54**). The second quantitative information is the determination of the unit cell parameters. For a hexagonal crystal system, the small deviations, observed for *a* and *c* (**Table S2**), are in accordance with the unit cell parameters calculated from low-dose HR-TEM refinement of the powder diffraction data (Rietveld method) and with cRED data.

Interestingly, as a preliminary attempt, following slightly similar synthetic conditions (details are given in the Supporting Information) the use of 2,5-dichlorotherephthalic acid yielded the isostructural phase MIP-209(Ti)-2Cl as revealed from the PXRD patterns (**Figure S18).** Although a similar pore size can be estimated from the DFT-optimized structures, the experimental N_2 uptake at 77 K is significantly lower than expected (**Figure S19 and S20**), likely due to residual impurities such as TiO_2, calling for further synthesis optimization. Even though other attempts to produce similar structures using other functionalized 1,4-BDC linkers, or even parent ligand, did not result yet in crystalline solids, MIP-209(Ti) represents, however, a very scare example of isostructural Ti-MOF type achieved using functional terephthalate ligands.

When analyzing the differences in terms of IBU for Ti-MOFs (**Table S3**), it is clear that any attempt to correlate them with differences in terms of synthesis conditions is still highly challenging. Ti carboxylate-based MOFs are constructed either from Ti_3 to Ti_{12} oxo-clusters or infinite chains of corner-sharing of Ti octahedra or more complex TiO_6 chains and 2D Ti oxide networks.[22,32] When it turns to Ti_8 or Ti_{12} IBUs, the resulting MOFs are obtained in pure carboxylic acids as solvent in solvothermal conditions, the corresponding IBUs combine carboxylates from the ligands and bridging or chelating formates or acetates. In the case of TiO chains or Ti_6O_9 nanowire chain-based MOFs, these are obtained in pure organic solvents under solvothermal conditions (DMF, DEF,

alcohols), without any formic or acetic acid that might compete for the chelation of the Ti species. One could therefore tentatively propose that the use of monocarboxylic acids as pure solvents, thus in very large excess when compared to the steochiometric polycarboxylic acids (ligands), favor the formation of "interrupted" Ti oxo-clusters networks such as Ti_8 or Ti_{12} IBUs. The lower nuclearity Ti clusters (Ti_3 or Ti_7)-based MOFs have been synthesized using mixtures of organic solvent and acids as modulators. When it comes to strongly complexing ligands such as carboxyphenolates or hydroxyamates, that compete with the inorganic condensation of Ti, one can form discrete Ti or Ti_2 IBUs. However, we cannot yet gain a complete rational analysis of the synthesized MOF. In fact, until recently every newly reported Ti carboxylate MOF exhibited a different IBU.[7] But interestingly, the very recent appearance of several Ti-MOFs bearing the same IBU (i.e., Ti_{12} clusters, Ti_6 chains) suggests the existence of chemical key parameters that have still to be precisely deciphered in order to develop rational design strategies of Ti-MOFs. In this regard, the MIP-177(Ti)-LT and MIP-209(Ti) represent one of the most extreme cases reported, so far, with similar Ti_{12} IBUs, while these materials are built from linkers with very different topicities (*i.e.*, tetra- versus dicarboxylates) and geometries (*i.e.*, pseudo-rectangular versus linear).

Modification of the inorganic moiety

The chemical and photochemical stability of MIP-209(Ti)-NO_2 was evaluated on the perspective of using this material in photocatalysis. After exposing the solid in different solvents for 24 h days (following a detailed protocol described in Supplementary Information), PXRD patterns revealed a significant decrease in crystallinity (*e.g.*, particle size decrease) and/or possible structural degradation (**Figure S21**). The FT-IR spectral analyses evidenced the generation of free carboxylic ligands when soaked into warm water or strong acids (**Figure S22**). Nitrogen isotherms measurements at 77 K (**Figure S23**) revealed about 15% decrease of gas uptake compared with MIP-209(Ti)-NO_2 before treatment. Compared to the tetra-carboxylate MIP-177(Ti)-LT, MIP-209(Ti)-NO_2 is relatively less stable in diverse various conditions. We hypothesize, from a purely qualitative point of view, the framework with tetratopic ligand could give a relatively high chemical stability against that with ditopic ligand on the same IBUs, as seen before in other systems such as Fe(III) polycarboxylates with MIL-88's and MIL-127, constructed from Fe_3O clusters and di or tetra-carboxylates, exhibiting strong differences in chemical stability.

To overcome this lack of chemical stability, we decided to dope MIP-209. In fact, the doping strategy with transition metal elements on the inorganic $Ti_{12}O_{15}$ cluster moiety has been recently reported[33,54], while the strong chemical inertness of Cr^{3+} ions make

this transition metal a promising candidate to enhance the water stability of MIP-209(Ti).[55,56] This, together with the proven ability of metal ion substitution onto the Ti_{12} oxo-cluster of MIP-177(Ti)-LT,[33] encouraged us to investigate the doping of the Ti-MOF through the direct synthesis relying on diverse chromium metal precursors like $Cr(NO_3)_3$, $CrCl_3$, while tuning the order of addition of each chemical, and other reaction conditions. Consequently, a Cr-doped MIP-209(Ti)-NO_2 sample, labeled as MIP-209(Ti-Cr)-NO_2, was obtained following a one-pot synthesis procedure and analysed by several characterization methods (**Figure S24-26**). A 5 at% Cr (versus Ti) doped MIP-209(Ti-Cr)-NO_2 was obtained with a very good reproducibility as shown by the systematic PXRD analysis. The sample purity was further assessed through a combination of advanced characterization techniques, namely HR-TEM imaging and energy-dispersed X-ray spectroscopy (EDX) mapping (**Figure S27 and S28**). Unfortunately, despite all our attempts, the MIP-209(Ti-Cr)-NO_2 sample has been always obtained with around 6 wt% titanium oxide impurity, as estimated from TGA and shown on HR-TEM images. Note that this oxide impurity contains about one order of magnitude less Cr element (0.5 at%) compared to MIP-209(Ti-Cr)-NO_2 as shown from EDX mapping.

The good water stability of MIP-209(Ti-Cr)-NO_2 was demonstrated under different conditions. In contrast with MIP-209(Ti)-NO_2, MIP-209(Ti-Cr)-NO_2 displayed relatively higher water tolerance and kept the high porosity after the same condition treatment. As observed by PXRD analysis (**Figure 3A**), the peak intensity was kept confirming the positive role of the Cr doping. Nitrogen sorption measurements further confirmed the enhanced stability after 7 days water treatment at room temperature, where the N_2 uptake was even slightly higher than that for the pristine MIP-209(Ti)-NO_2 and MIP-209(Ti-Cr)-NO_2 (**Figure 3B**). The tiny (positive) deviation is probably ascribed to the removal of free residual ligand or acetates after soaking the MOF for such a long period of time. To better understand this, a series of additional characterization measurements, including FT-IR, TGA, ^1H nuclear magnetic resonance, and SEM/EDX energy-dispersed X-ray spectroscopy (**Figure S29-33**), confirmed this hypothesis with the release of ligands and acetates from MIP-209(Ti-Cr)-NO_2 during this water treatment as shown in **Figure S34**, leading to a 17% increase of the porosity (while the removal of acetates in the case of MIP-209(Ti)-NO_2 seems to be detrimental leading to a 20% loss of the porosity). Motivated by the enhanced water stability of MIP-209(Ti-Cr)-NO_2, the accessibility of Ti-centers on the IBUs and the associated intrinsic photo-redox activity, the potential of this MOF for the photocatalytic hydrogen evolution reaction from water was further investigated.

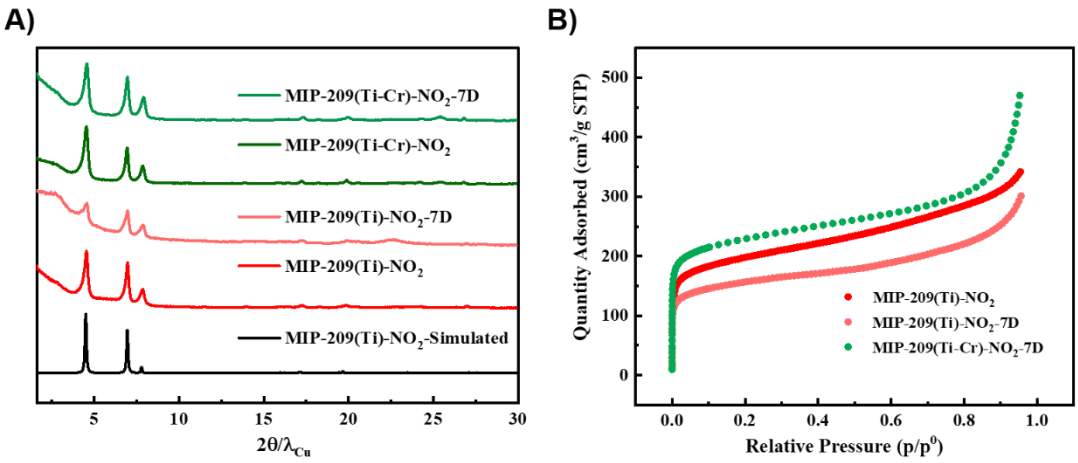

Figure 3. Water stability test results for MIP-209(Ti)-NO_2 and MIP-209(Ti-Cr)-NO_2 ([Cr] = 5 at%). A) PXRD patterns and B) nitrogen adsorption isotherms before and after water treatment (soaked in water for 7 days). (The hump at 22.5 degree observed on PXRD patterns is due to the sample holder).

Photocatalytic hydrogen evolution

Prior to any photocatalytic reaction investigation, the UV-Vis absorption spectra for MIP-209(Ti)-NO_2 and MIP-209(Ti-Cr)-NO_2 were first recorded in the diffuse reflectance mode (**Figure S35**). The optical band gaps of MIP-209(Ti)-NO_2 and MIP-209(Ti-Cr)-NO_2 estimated from the Tauc plots are 3.46 and 3.34 eV, respectively (**Figure S36**). This result indicates that Cr doping slightly narrows the band gap of MIP-209(Ti)-NO_2, thus, increasing the light harvesting ability. Apparently, Cr doping on Ti-MOF replaces Ti atoms in the lattice with oxygen vacancy compensation, distributed homogeneously in the framework, resulting in a red shift of the absorption onset. The composition and oxidation state of the elements present in these Ti-MOFs were determined by X-ray photoelectron spectroscopy (XPS), (see **Figure S37 and S38)**. The C1s spectrum shows the specific signal of the C-NO_2 present in the nitro terephthalate ligand (~286 eV). Note here that the high COO^- energy value (~288 eV) might correspond to some acetate moieties remaining from the synthesis. The O1s spectrum exhibits two components, a broader one about ~532 eV characteristic of the oxygen atoms present in the carboxylate and nitro groups as well as Ti(IV)-O bonds in inorganic metal nodes, and another one at about ~530 eV due to the Ti(IV)-OH. The N1s spectrum exhibits two peaks, one corresponding to the nitrogen atoms in the NO_2 group present in the MIP-209, at about ~405 eV and a second minor component (22 % atomic percentage) due to the N atoms formed in the spontaneous reduction of the nitro to the amino group. Similar observations have been reported in the case of UiO-66(Zr)-NO_2 preparation from 2-nitroterephthalte and observing that the resulting MOF exhibits some

spectroscopic features characteristic of NH_2 groups.[57] The Ti2p spectrum shows two bands attributable to the Ti $2p_{3/2}$ (~458 eV) and Ti $2p_{1/2}$ bands (~464 eV), characteristic of the Ti^{4+} ions present in the $Ti_{12}O_{15}$ cluster. The XPS Cr 2p peak indicates the presence of Cr^{3+} ions in the SBU, as revealed by the Cr $2p_{3/2}$ (~577 eV) and $2p_{1/2}$ (~587 eV).

XPS was also used to determine the highest occupied crystal orbital (HOCO) energy maximum of MIP-209(Ti)-NO_2 and MIP-209(Ti-Cr)-NO_2 by monitoring the first emitted electron band energy in the materials by determining the intersection between extrapolation of the linear portion of this lowest energy emission edge and the background (**Figure S39A-B**). The obtained value corresponds to the HOCO energy versus the Fermi level (E^f_u). The HOCO position versus the NHE (E_u^{NHE}) can be obtained from the following equation: $E_u^{NHE} = E^f_u + \phi_{sp} - 4.44$, where ϕ_{sp} is the work function of the spectrometer calibrated against Au, Ag and Cu foils as reference that has a value of 4.244 eV. From this Eu^{NHE} value and the band gap, the lowest unoccupied crystal orbital (LUCO) band energy minimum (E_c^{NHE}) can be determined. As shown in **Figure S39C**, both materials meet the thermodynamic requirement to be used as photocatalysts for the OWS. Especially, MIP-209(Ti-Cr)-NO_2 exhibits a slightly lower band gap and more positive LUCO value in comparison with MIP-209(Ti)-NO_2.

The photocatalytic activity of MIP-209(Ti) materials was then evaluated for both HER and OWS under simulated sunlight irradiation at 20 °C. To set the photocatalytic activity of MIP-209(Ti) materials in a broader context, standard P25 TiO_2 was also used as reference photocatalyst for HER in the presence of methanol as hole scavenger. The results obtained using MIP-209(Ti)-NO_2, MIP-209(Ti-Cr)-NO_2 and P25 as photocatalysts for HER under identical conditions are shown in **Figure 4A**. Although MIP-209(Ti)-NO_2 showed significant activity in HER (ca. 4750 μmol H_2/g_{cat} in 5 h), it was observed that the material loses its crystallinity in a large extent as determined by PXRD of the used MIP-209(Ti)-NO_2 sample after 5 h irradiation (**Figure S40**). Interestingly, MIP-209(Ti-Cr)-NO_2 also exhibited an even higher hydrogen production (5812 μmol H_2/g_{cat} in 5 h) than MIP-209(Ti)-NO_2 while exhibiting higher stability as revealed by PXRD (**Figure S40**). In addition, negligible metal leaching was detected when using MIP-209(Ti-Cr)-NO_2 as photocatalyst (0.01 and <0.001 mg/L for Cr and Ti, respectively).

Since MIP-209(Ti-Cr)-NO_2 may contain some TiO_2 anatase impurity (about 6 % weight), a control using P25 TiO_2 as photocatalyst was performed. It was observed that under the current reaction conditions, P25 evolves 2609 μmol H_2/g_{cat}, that is about one half

the H_2 amount evolved by MIP-209(Cr-Ti)-NO_2. Although a synergistic effect of interfaced TiO_2/MIP-209(Ti-Cr)-NO_2 cannot be excluded, precedents in the literature have shown that this type of host/guest systems does not exhibit such a big increase in photocatalytic activity.[58,59]

In photocatalytic OWS reaction, MIP-209(Ti-Cr)-NO_2 without precious metal nanoparticles as co-catalysts exhibits under simulated solar light irradiation hydrogen production accompanied by the corresponding stoichiometric amount of oxygen (681 μmol H_2/g_{cat} and 325 μmol O_2/g_{cat} in 5 h at 20 °C) (**Figure 4B**). Similar photocatalytic activity was achieved when the reaction is carried out at 10 ºC (**Figure S41**). In addition, a photocatalytic control experiment using labelled $H_2{}^{18}O$ and gas analysis by GC-MS revealed the formation of $^{18}O_2$ (m/z 36), therefore, confirming the occurrence of photocatalytic water oxidation by MIP-209(Ti-Cr)-NO_2 (**Figure S42**). These values of gas evolution in OWS obtained using this Ti-MOF are remarkable and compare well with previous data reported in the literature,[60] with the advantage in the present case that the MIP-209(Ti-Cr)-NO_2 does not contain any precious metal as co-catalyst. Importantly, MIP-209(Ti-Cr)-NO_2 shows about 6-fold times higher activity than IEF-11 framework[22] taken as benchmark (H_2 and O_2 94 and 53 μmol g^{-1}, respectively) under same reaction conditions (5 mg of photocatalyst, 20 mL H_2O, 10 ºC, 5 h reaction time, simulated sunlight irradiation). As commented, MIP-209(Ti-Cr)-NO_2 maintains a higher crystallinity after three times uses for HER tests, retaining a better crystallinity, in comparison to MIP-209(Ti)-NO_2. Similarly, while MIP-209(Ti)-NO_2 becomes totally amorphous after the OWS test, MIP-209(Ti-Cr)-NO_2 still displays crystallinity, in agreement with the positive structural reinforcement effect of Cr doping on the stability of this MOF. UV (**Figure S35**) and XPS analyses (**Figure S43 and S44**) of the solids after OWS reaction were performed to compare these data with those of the fresh samples. In addition, low metal leaching was measured for MIP-209(Ti-Cr)-NO_2, obtaining values of 0.284 and 0.084 mg/L of Cr and Ti, respectively, as evidenced by ICP-OES analyses of the liquid phase after the reaction.

Two additional MIP-209(Ti-Cr)-NO_2 samples with diminished Cr content were also prepared (1 at% and 2.5 at%) in order to determine the best compromise between the structural stabilization effect of Cr and their photocatalytic activity for HER and OWS (data not shown). The decrease in the Cr content from 5 to 2.5 or 1 at% does not play a significant influence on the photocatalytic activity for HER or OWS, while this lower Cr percentage still having a positive effect on the crystallinity of the material after use. The PXRD data for the samples used as photocatalysts under simulated sunlight irradiation are presented in **Figure S45**. Thus, these measurements after irradiation in

the presence of methanol for 1 or 2.5 at% Cr show a negligible decrease in the crystallinity, suggesting that just a smaller amount of Cr could be enough to promote a notable structural stability. In contrast, conditions of OWS tests were more damaging from the stability point of view, leading to a significant decrease in the crystallinity of the resulting material, both at 1 or 2.5 at% Cr content in the sample. This suggests that photogenerated holes in these materials are more detrimental for the structure stability, while photogenerated electrons have lesser influence in structural stability. It can be proposed that due to the weaker coordination of the carboxylate linker caused by the inductive and resonance effect of the nitro group, holes presumably at the carboxylate ligand, further decrease the strength of the coordinative metal-ligand bond that eventually leads its hydrolysis causing structural damage. The proposal is illustrated in Scheme **S46**.

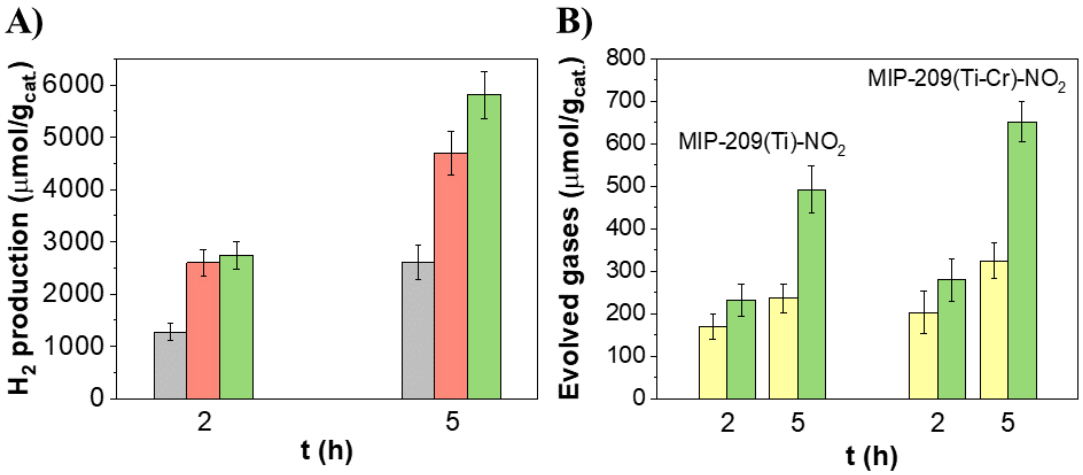

Figure 4. (A) Photocatalytic HER in the presence of methanol under simulated sunlight irradiation of MIP-209(Ti)-NO_2 (red) and MIP-209(Ti-Cr)-NO_2 (green; [Cr] = 5 at%)) in comparison with TiO_2-P25 (grey). Reaction conditions: 5 mg of photocatalyst in a 20 mL mixture of milliQ H_2O and MeOH (5:1) at 20 ºC. (B) Photocatalytic OWS of MIP-209(Ti)-NO_2 and MIP-209(Ti-Cr)-NO_2 under simulated sunlight irradiation. Legend colors: yellow, O_2 production; green, H_2 production. Reaction conditions: 5 mg of photocatalyst in a 20 mL mixture of milliQ H_2O at 20 ºC.

Considering that MIP-209(Ti) contains in its structure $Ti_{12}O_{15}$ oxo-clusters that are also present in MIP-177(Ti)-LT, it was of interest to determine their relative photocatalytic activity for OWS under simulated sunlight irradiation as well as the structural stability of the latter, knowing that this MOF has also demonstrated remarkable activity for the photocatalytic dehydrogenation of formic acid.[61] The results obtained in H_2 and O_2 evolution in OWS, using MIP-177(Ti)-LT as photocatalyst, were almost coincident at 2 and 5 h with those achieved with MIP-209(Ti-Cr)-NO_2 (**Figure S47**). The main advantage of MIP-177(Ti)-LT[33,61] in respect to MIP-209(Ti-Cr)-NO_2 appears to be its higher structural stability under reaction conditions in aqueous medium. Thus, PXRD

of the MIP-177(Ti)-LT after the photocatalytic test (**Figure S48**) shows that the crystal structure has been well preserved. Also, XPS analysis of the used MIP-177(Ti)-LT sample (**Figure S50**) was coincident with data of the fresh material (**Figure S49**) indicating that there are no changes in the oxidation state or coordination sphere of the elements present in MIP-177(Ti)-LT after irradiation. This finding highlights the potential of the $Ti_{12}O_{15}$ oxo-cluster for the photocatalytic hydrogen production from water. Therefore, with the possibilities of doping this IBU and modifying the organic ligands, either by exchanging the non-bridging formates/acetates groups or by playing on the nature of the organic linkers, this family of Ti_{12}-based MOFs opens the doors for promising discoveries towards sustainable photocatalytic hydrogen production.

Mechanism of photocatalytic reaction

Periodic Density Functional Theory (DFT) calculations were further performed to shed light on the HER reaction mechanism to identify the electronic and structural features of MIP-209(Ti)-NO_2 responsible for its catalytic performance (all details provided in Supporting Information, **Figure S51-53**). The *H adsorption configurations were first explored and reported in **Figure 5A**, in which for sake of clarity only the region of the $Ti_{12}O_{15}$ oxo-cluster is drawn. The Ti sites initially coordinated to H_2O (site I) were considered as the potential catalytic active sites. The corresponding simulated free energy profiles indicate that the hydrogen adsorption on this site-I is endothermic and the ΔG_H averaged over the *H configurations interacting with the three Ti sites is 1.04 eV (**Figure 5B**). For comparison, the ΔG_H calculated for the benchmark TiO_2 (110) (0.37 eV) (**Figure 5B**) is much lower that makes site-I likely not catalytically active. We therefore considered an alternative Ti atom potentially exposed (site-II) due to the missing acetate moieties as observed experimentally, leading to a ΔG_H of 0.79 eV lower as compared to the value obtained for site-I. Therefore, although the so-obtained ΔG_H for site II remains above the corresponding value for TiO_2, this ΔG_H falls in the range of values (0.6-0.8 eV) previously calculated for other catalysts with experimentally demonstrated good HER activity[62]. The free energy profiles and resulting ΔG_H values for site-I and site-II in the periodic MIP-209(Ti)-2Cl structures as well as in $Ti_{12}O_{15}$ oxo-cluster are equally provided in **Figure S55.** This additional set of calculations confirmed that site-II is predicted to be the most active sites in all scenarios with ΔG_H ranging from 0.56 to 0.62 eV that makes these MIP-209(Ti) variants also catalytically active. Charge density difference analysis on MIP-209(Ti)-NO_2 with the site-II adsorption configuration, demonstrated that there is an accumulation of electrons on the H adsorbate with a corresponding Bader charge of 0.42 *e* (**Figure 5C**), this effective electron transfer being beneficial for the hydrogen adsorption.

Furthermore, to reveal the origin of hydrogen affinity, partial density of states (pDOS) analysis of the *sd* orbital overlapping of the Ti-H interaction (**Figure 5D**), revealed a Ti-H covalent character (overall total DOS in **Figure S56**). Additional, crystal orbital Hamilton populations (COHP)[63] identified that the strength of Ti-H interaction stems from the binding below the Fermi energy level and anti-bonding above the Fermi energy level. The tendency of binding strength uncovered by the integrated COHP (ICOPH) values is consistent with the ΔG_H variation (**Figure 5E**).

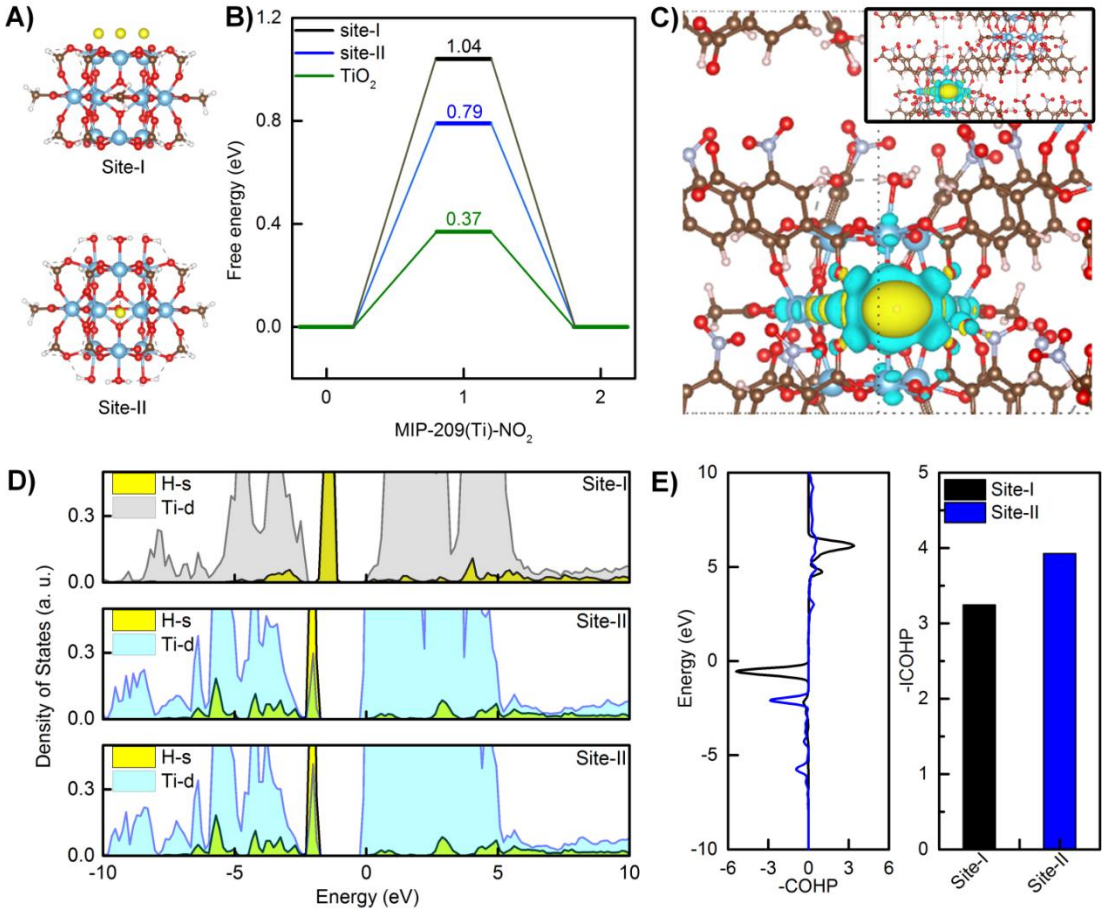

Figure 5. (A) Illustrations of the DFT-optimized *H adsorption configurations on site-I and site-II of MIP-209(Ti)-NO_2. The color scheme: H, white; C, brown; N, silvery white; O, red; Ti, blue; *H adsorbate, yellow. (B) DFT-derived Gibbs free energy profile for HER reaction by MIP-209(Ti)-NO_2. The average ΔG_H on site-I is adopted considering the three exposed Ti atoms. (C) Deformation charge density of *H adsorption on site-II for MIP-209(Ti)-NO_2. Yellow and blue correspond to the electron accumulation and electron depletion. (D) Partial Density of States (DOS) between H-*s* band and Ti-*d* band for *H adsorption on MIP-209(Ti)-NO_2. The Fermi level is at 0 eV. (E) Crystal orbital Hamilton populations (COHP) of *H adsorption on MIP-209(Ti)-NO_2 and Integrated crystal orbital Hamilton populations (ICOPH) of Ti-H interaction. The Fermi level is at 0 eV. Positive and negative values of COHP correspond to the bonding and antibonding interactions.

Therefore, the ability of Ti sites to strongly adsorb hydrogen stems from the formation of a Ti-H covalent bonding as it was already mentioned in the case of TiO_2.[64] The same conclusion can be drawn from the analysis of the $Ti_{12}O_{15}$ cluster and MIP-209(Ti)-2Cl (**Table S4**). This whole analysis supports that the exposed Ti sites resulting from the absence of acetate moieties play a key role in the whole photocatalytic hydrogen evolution of MIP-209(Ti)-NO_2 and its derivatives.

Conclusions

A novel isostructural Ti-MOF, MIP-209(Ti)-X (X = NO_2 or 2Cl), bearing $Ti_{12}O_{15}$ oxo-clusters and terephthalate derivatives, was obtained via a green solvothermal synthesis route. Through a combination of synchrotron PDF analysis, cRED, and HR-TEM, the structure of MIP-209(Ti)-NO_2 was successfully determined and refined using high-resolution PXRD. Owing to the tunability of the Ti_{12}-IBU, Cr^{3+} ion was used to partially replace Ti^{4+} centers (up to ca. 5%) in a uniform manner which significantly enhanced the water stability of the framework, in particular under light irradiation. Markedly, the MIP-209-NO_2 demonstrated a significantly hydrogen production rate from water with relatively good reusability and stability in both HER and OWS reactions under simulated sunlight irradiation (5812 and 681 µmol of H_2/g_{cat} in 5 h, respectively). Besides, the potential and activity of the Ti_{12} oxo-clusters was also supported by means of DFT calculations, revealing that the Ti-sites are likely to prevail for hydrogen evolution, thanks to suitable Ti-H binding energy levels, regardless the nature of the organic linker. These results on MIP-209(Ti-Cr)-NO_2 attest the potential of $Ti_{12}O_{15}$ IBU as platform for photocatalytic hydrogen production and energy related applications. Therefore, this work represents another leap forward in the rational design and discovery of porous functional Ti-MOFs with important photo-responsive applications.

Acknowledgments

The authors acknowledge the European Union under the Grant Agreement 101084131 (MOF2H2 project) for the financial support, and the CNRS-CEA “METSA” French network (FR CNRS 3507) on the platform IRMA (CRISMAT-Caen) for the support in cRED data collection and analysis. The CRISTAL beamline staff members from Soleil synchrotron are acknowledged for the high-energy powder X-ray diffraction data. H.G. thanks financial support by the Spanish Ministry of Science and Innovation (CEX-2021-001230-S and PDI2021-0126071-OB-CO21 funded by MICIU/AEI/ 10.13039/501100011033) and Generalitat Valenciana (Prometeo 2021/038 and Advanced Materials programme Graphica MFA/2022/023 with funding from European Union NextGenerationEU PRTR-C17.I1). S.N. thanks the support of grant PID2021-123856OBI00 funded by MICIU/AEI/10.13039/501100011033 and by ERDF A way of making Europe. The computational work was performed using HPC resources from GENCI-CINES (Grant A0160907613).

Author contributions

B. C. worked on the synthesis and characterization of the MOF samples. A. M., I. D., P. B., and G. P. worked on the structure determination, low dose HR-TEM and synchrotron PDF analysis. A. M. and L. A. F. worked on the metal doping synthesis. C. M. R., S. N., H. G. measured the photocatalytic tests. B. X., D. F., and G. M. performed the DFT simulations. G. M. and C. S. supervised the work and all co-authors contributed to the manuscript writing.

References

(1) Wang, Q.; Domen, K. Particulate Photocatalysts for Light-Driven Water Splitting: Mechanisms, Challenges, and Design Strategies. *Chemical Reviews* **2020**, *120*, 919-985.

(2) Chen, S.; Takata, T.; Domen, K. Particulate photocatalysts for overall water splitting. *Nature Reviews Materials* **2017**, *2*, 17050.

(3) Tao, X.; Zhao, Y.; Wang, S.; Li, C.; Li, R. Recent advances and perspectives for solar-driven water splitting using particulate photocatalysts. *Chemical Society Reviews* **2022**, *51*, 3561-3608.

(4) Rahman, M. Z.; Edvinsson, T.; Gascon, J. Hole utilization in solar hydrogen production. *Nature Reviews Chemistry* **2022**, *6*, 243-258.

(5) Jaryal, R.; Kumar, R.; Khullar, S. Mixed metal-metal organic frameworks (MM-MOFs) and their use as efficient photocatalysts for hydrogen evolution from water splitting reactions. *Coordination Chemistry Reviews* **2022**, *464*, 214542.

(6) Chen, X.; Liu, L.; Yu, P. Y.; Mao, S. S. Increasing Solar Absorption for Photocatalysis with Black Hydrogenated Titanium Dioxide Nanocrystals. *Science* **2011**, *331*, 746-750.

(7) Assi, H.; Mouchaham, G.; Steunou, N.; Devic, T.; Serre, C. Titanium coordination compounds: from discrete metal complexes to metal–organic frameworks. *Chemical Society Reviews* **2017**, *46*, 3431-3452.

(8) Li, L.; Wang, X.-S.; Liu, T.-F.; Ye, J. Titanium-Based MOF Materials: From Crystal Engineering to Photocatalysis. *Small Methods* **2020**, *4*, 2000486.

(9) Yan, Y.; Li, C.; Wu, Y.; Gao, J.; Zhang, Q. From isolated Ti-oxo clusters to infinite Ti-oxo chains and sheets: recent advances in photoactive Ti-based MOFs. *Journal of Materials Chemistry A* **2020**, *8*, 15245-15270.

(10) Kolobov, N.; Goesten, M. G.; Gascon, J. Metal–Organic Frameworks: Molecules or Semiconductors in Photocatalysis? *Angewandte Chemie International Edition* **2021**, *60*, 26038-26052.

(11) Serre, C.; Férey, G. Hybrid Open Frameworks. 8. Hydrothermal Synthesis, Crystal Structure, and Thermal Behavior of the First Three-Dimensional Titanium(IV) Diphosphonate with an Open Structure: Ti3O2(H2O)2(O3P−(CH2)−PO3)2·(H2O)2, or MIL-22. *Inorganic chemistry* **1999**, *38*, 5370-5373.

(12) Serre, C.; Férey, G. Hydrothermal Synthesis and Structure Determination from Powder Data of New Three-Dimensional Titanium(IV) Diphosphonates Ti(O3P−(CH2)n−PO3) or MIL-25n (n = 2, 3). *Inorganic chemistry* **2001**, *40*, 5350-5353.

(13) Serre, C.; Groves, J. A.; Lightfoot, P.; Slawin, A. M. Z.; Wright, P. A.; Stock, N.; Bein, T.; Haouas, M.; Taulelle, F.; Férey, G. Synthesis, Structure and Properties of Related Microporous N,N'-Piperazinebismethylenephosphonates of Aluminum and Titanium. *Chemistry of Materials* **2006**, *18*, 1451-1457.

(14) Lu, L.; Wu, B.; Shi, W.; Cheng, P. Metal–organic framework-derived heterojunctions as nanocatalysts for photocatalytic hydrogen production. *Inorganic Chemistry Frontiers* **2019**, *6*, 3456-3467.

(15) Li, C.; Xu, H.; Gao, J.; Du, W.; Shangguan, L.; Zhang, X.; Lin, R.-B.; Wu, H.; Zhou, W.; Liu, X. Tunable titanium metal–organic frameworks with infinite 1D Ti–O rods for efficient visible-light-driven photocatalytic H 2 evolution. *Journal of Materials Chemistry A* **2019**, *7*, 11928-11933.

(16) Song, Y.; Li, Z.; Zhu, Y.; Feng, X.; Chen, J. S.; Kaufmann, M.; Wang, C.; Lin, W. Titanium hydroxide secondary building units in metal–organic frameworks catalyze hydrogen evolution under visible light. *Journal of the American Chemical Society* **2019**, *141*, 12219-12223.

(17) Wang, X.; Zhang, X.; Zhou, W.; Liu, L.; Ye, J.; Wang, D. An ultrathin porphyrin-based metal-organic framework for efficient photocatalytic hydrogen evolution under visible light. *Nano Energy* **2019**, *62*, 250-258.

(18) Kolobov, N.; Zaki, A.; Świrk, K.; Maity, P.; Garzon-Tovar, L.; Angeli, G. K.; Dikhtiarenko, A.; Delahay, G.; Trikalitis, P. N.; Emwas, A.-H. Understanding Photocatalytic Activity Dependence on Node Topology in Ti-Based Metal–Organic Frameworks. *ACS Materials Letters* **2023**, *5*, 1481-1487.

(19) Meyer, K.; Ranocchiari, M.; van Bokhoven, J. A. Metal organic frameworks for photo-catalytic water splitting. *Energy & Environmental Science* **2015**, *8*, 1923-1937.

(20) Nguyen, H. L. Metal–organic frameworks for photocatalytic water splitting. *Solar RRL* **2021**, *5*, 2100198.

(21) Remiro-Buenamanana, S.; Cabrero-Antonino, M.; Martinez-Guanter, M.; Alvaro, M.; Navalon, S.; Garcia, H. Influence of co-catalysts on the photocatalytic activity of MIL-125 (Ti)-NH2 in the overall water splitting. *Applied Catalysis B: Environmental* **2019**, *254*, 677-684.

(22) Salcedo-Abraira, P.; Babaryk, A. A.; Montero-Lanzuela, E.; Contreras-Almengor, O. R.; Cabrero-Antonino, M.; Grape, E. S.; Willhammar, T.; Navalón, S.; Elkäim, E.; García, H. A Novel Porous Ti-Squarate as Efficient Photocatalyst in the Overall Water Splitting Reaction under Simulated Sunlight Irradiation. *Advanced Materials* **2021**, *33*, 2106627.

(23) An, Y.; Xu, B.; Liu, Y.; Wang, Z.; Wang, P.; Dai, Y.; Qin, X.; Zhang, X.; Huang, B. Photocatalytic Overall Water Splitting over MIL-125 (Ti) upon CoPi and Pt Co-catalyst Deposition. *ChemistryOpen* **2017**, *6*, 701-705.

(24) Li, R.; Zhang, W.; Zhou, K. Metal–Organic-Framework-Based Catalysts for Photoreduction of CO2. *Advanced Materials* **2018**, *30*, 1705512.

(25) McNamara, N. D.; Neumann, G. T.; Masko, E. T.; Urban, J. A.; Hicks, J. C. Catalytic performance and stability of (V) MIL-47 and (Ti) MIL-125 in the oxidative desulfurization of heterocyclic aromatic sulfur compounds. *Journal of catalysis* **2013**, *305*, 217-226.

(26) Wang, H.; Yuan, X.; Wu, Y.; Zeng, G.; Chen, X.; Leng, L.; Li, H. Synthesis and applications of novel graphitic carbon nitride/metal-organic frameworks mesoporous photocatalyst for dyes removal. *Applied Catalysis B: Environmental* **2015**, *174*, 445-454.

(27) Freund, R.; Zaremba, O.; Arnauts, G.; Ameloot, R.; Skorupskii, G.; Dincă, M.; Bavykina, A.; Gascon, J.; Ejsmont, A.; Goscianska, J. The current status of MOF and COF applications. *Angewandte Chemie International Edition* **2021**, *60*, 23975-24001.

(28) Melillo, A.; Cabrero-Antonino, M.; Navalon, S.; Alvaro, M.; Ferrer, B.; Garcia, H. Enhancing visible-light photocatalytic activity for overall water splitting in UiO-66 by controlling metal node composition. *Applied Catalysis B: Environmental* **2020**, *278*, 119345.

(29) Yuan, S.; Qin, J.-S.; Xu, H.-Q.; Su, J.; Rossi, D.; Chen, Y.; Zhang, L.; Lollar, C.; Wang, Q.; Jiang, H.-L.; Son, D. H.; Xu, H.; Huang, Z.; Zou, X.; Zhou, H.-C. [Ti8Zr2O12 (COO) 16] Cluster: an ideal inorganic building unit for photoactive metal–organic frameworks. *ACS central science* **2018**, *4*, 105-111.

(30) Hong, K.; Chun, H. Unprecedented and highly symmetric (6, 8)-connected topology in a porous metal–organic framework through a Zn–Ti heterometallic approach. *Chemical Communications* **2013**, *49*, 10953-10955.

(31) Fang, W.-H.; Zhang, L.; Zhang, J. Synthetic strategies, diverse structures and tuneable properties of polyoxo-titanium clusters. *Chemical Society Reviews* **2018**, *47*, 404-421.

(32) Yan, Q.; Wang, J.; Zhang, L.; Liu, J.; Wahiduzzaman, M.; Yan, N.; Yu, L.; Dupuis, R.; Wang, H.; Maurin, G.; Hirscher, M.; Guo, P.; Wang, S.; Du, J. A

squarate-pillared titanium oxide quantum sieve towards practical hydrogen isotope separation. *Nature Communications* **2023**, *14*, 4189.

(33) Wang, S.; Kitao, T.; Guillou, N.; Wahiduzzaman, M.; Martineau-Corcos, C.; Nouar, F.; Tissot, A.; Binet, L.; Ramsahye, N.; Devautour-Vinot, S. A phase transformable ultrastable titanium-carboxylate framework for photoconduction. *Nature communications* **2018**, *9*, 1-9.

(34) Wang, S.; Reinsch, H.; Heymans, N.; Wahiduzzaman, M.; Martineau-Corcos, C.; De Weireld, G.; Maurin, G.; Serre, C. Toward a rational design of titanium metal-organic frameworks. *Matter* **2020**, *2*, 440-450.

(35) Wang, S.; Cabrero-Antonino, M.; Navalón, S.; Cao, C.-c.; Tissot, A.; Dovgaliuk, I.; Marrot, J.; Martineau-Corcos, C.; Yu, L.; Wang, H. A robust titanium isophthalate metal-organic framework for visible-light photocatalytic CO2 methanation. *Chem* **2020**, *6*, 3409-3427.

(36) Wang, S.; Chen, L.; Wahiduzzaman, M.; Tissot, A.; Zhou, L.; Ibarra, I. A.; Gutiérrez-Alejandre, A.; Lee, J. S.; Chang, J.-S.; Liu, Z. A mesoporous zirconium-isophthalate multifunctional platform. *Matter* **2021**, *4*, 182-194.

(37) Li, C.; Xu, H.; Gao, J.; Du, W.; Shangguan, L.; Zhang, X.; Lin, R.-B.; Wu, H.; Zhou, W.; Liu, X.; Yao, J.; Chen, B. Tunable titanium metal–organic frameworks with infinite 1D Ti–O rods for efficient visible-light-driven photocatalytic H2 evolution. *Journal of Materials Chemistry A* **2019**, *7*, 11928-11933.

(38) Zlotea, C.; Phanon, D.; Mazaj, M.; Heurtaux, D.; Guillerm, V.; Serre, C.; Horcajada, P.; Devic, T.; Magnier, E.; Cuevas, F. Effect of NH 2 and CF 3 functionalization on the hydrogen sorption properties of MOFs. *Dalton transactions* **2011**, *40*, 4879-4881.

(39) Fu, Y.; Sun, D.; Chen, Y.; Huang, R.; Ding, Z.; Fu, X.; Li, Z. An amine-functionalized titanium metal–organic framework photocatalyst with visible-light-induced activity for CO2 reduction. *Angewandte Chemie International Edition* **2012**, *51*, 3364-3367.

(40) Bryant, J. T.; Logan, M. W.; Chen, Z.; Djokic, M.; Cairnie, D. R.; Vazquez-Molina, D. A.; Nijamudheen, A.; Langlois, K. R.; Markley, M. J.; Pombar, G. Synergistic Steric and Electronic Effects on the Photoredox Catalysis by a Multivariate Library of Titania Metal–Organic Frameworks. *Journal of the American Chemical Society* **2023**, *145*, 4589-4600.

(41) Nguyen, H. L.; Vu, T. T.; Le, D.; Doan, T. L.; Nguyen, V. Q.; Phan, N. T. A titanium–organic framework: engineering of the band-gap energy for photocatalytic property enhancement. *ACS Catalysis* **2017**, *7*, 338-342.

(42) Deng, H.; Doonan, C. J.; Furukawa, H.; Ferreira, R. B.; Towne, J.; Knobler, C. B.; Wang, B.; Yaghi, O. M. Multiple functional groups of varying ratios in metal-organic frameworks. *Science* **2010**, *327*, 846-850.

(43) Castells-Gil, J.; Padial, N. M.; Almora-Barrios, N.; Albero, J.; Ruiz-Salvador, A. R.; González-Platas, J.; García, H.; Martí-Gastaldo, C. Chemical Engineering of Photoactivity in Heterometallic Titanium–Organic Frameworks by Metal Doping. *Angewandte Chemie International Edition* **2018**, *57*, 8453-8457.

(44) Lerma-Berlanga, B.; Castells-Gil, J.; Ganivet, C. R.; Almora-Barrios, N.; González-Platas, J.; Fabelo, O.; Padial, N. M.; Martí-Gastaldo, C. Permanent Porosity in Hydroxamate Titanium–Organic Polyhedra. *Journal of the American Chemical Society* **2021**, *143*, 21195-21199.

(45) Keum, Y.; Park, S.; Chen, Y. P.; Park, J. Titanium-Carboxylate Metal-Organic Framework Based on an Unprecedented Ti-Oxo Chain Cluster. *Angewandte Chemie* **2018**, *130*, 15068-15072.

(46) Yuan, S.; Liu, T.-F.; Feng, D.; Tian, J.; Wang, K.; Qin, J.; Zhang, Q.; Chen, Y.-P.; Bosch, M.; Zou, L. A single crystalline porphyrinic titanium metal–organic framework. *Chemical science* **2015**, *6*, 3926-3930.

(47) Cadiau, A.; Kolobov, N.; Srinivasan, S.; Goesten, M. G.; Haspel, H.; Bavykina, A. V.; Tchalala, M. R.; Maity, P.; Goryachev, A.; Poryvaev, A. S. A titanium

metal–organic framework with visible-light-responsive photocatalytic activity. *Angewandte Chemie* **2020**, *132*, 13570-13574.

(48) Dorset, D. L.; Hauptman, H. A. Direct phase determination for quasi-kinematical electron diffraction intensity data from organic microcrystals. *Ultramicroscopy* **1976**, *1*, 195-201.

(49) Dorset, D. L. Electron crystallography–accomplishments and challenges. *Acta Crystallographica Section A: Foundations of Crystallography* **1998**, *54*, 750-757.

(50) Yang, T.; Willhammar, T.; Xu, H.; Zou, X.; Huang, Z. Single-crystal structure determination of nanosized metal–organic frameworks by three-dimensional electron diffraction. *Nature Protocols* **2022**, 1-25.

(51) Smolders, S.; Willhammar, T.; Krajnc, A.; Sentosun, K.; Wharmby, M. T.; Lomachenko, K. A.; Bals, S.; Mali, G.; Roeffaers, M. B.; De Vos, D. E. A Titanium (IV)-Based Metal–Organic Framework Featuring Defect-Rich Ti-O Sheets as an Oxidative Desulfurization Catalyst. *Angewandte Chemie* **2019**, *131*, 9258-9263.

(52) Gemmi, M.; Mugnaioli, E.; Gorelik, T. E.; Kolb, U.; Palatinus, L.; Boullay, P.; Hovmöller, S.; Abrahams, J. P. 3D Electron Diffraction: The Nanocrystallography Revolution. *ACS central science* **2019**, *5*, 1315-1329.

(53) Rodríguez-Carvajal, J. Recent advances in magnetic structure determination by neutron powder diffraction. *Physica B: Condensed Matter* **1993**, *192*, 55-69.

(54) Murillo, B.; Zornoza, B.; de la Iglesia, O.; Wang, S.; Serre, C.; Téllez, C.; Coronas, J. Tin-Carboxylate MOFs for Sugar Transformation into Methyl Lactate. *European Journal of Inorganic Chemistry* **2019**, *2019*, 2624-2629.

(55) Bosch, M.; Zhang, M.; Zhou, H.-C. Increasing the stability of metal-organic frameworks. *Adv. Chem* **2014**, *2014*, 1155.

(56) An, Y.; Liu, Y.; Wang, Z.; Wang, P.; Zheng, Z.; Dai, Y.; Qin, X.; Zhang, X.; Whangbo, M.-H.; Huang, B. Stabilizing the titanium-based metal organic frameworks in water by metal cations with empty or partially-filled d orbitals. *Journal of colloid and interface science* **2019**, *533*, 9-12.

(57) Rueda-Navarro, C. M.; Abou Khalil, Z.; Melillo, A.; Ferrer, B.; Montero, R.; Longarte, A.; Daturi, M.; Vayá, I.; El-Roz, M.; Martínez-Martínez, V.; Baldoví, H. G.; Navalón, S. Solar Gas-Phase CO2 Hydrogenation by Multifunctional UiO-66 Photocatalysts. *ACS Catalysis* **2024**, *14*, 6470-6487.

(58) Dhakshinamoorthy, A.; Li, Z.; Garcia, H. Catalysis and photocatalysis by metal organic frameworks. *Chemical Society Reviews* **2018**, *47*, 8134-8172.

(59) He, X.; Ding, Y.; Huang, Z.; Liu, M.; Chi, M.; Wu, Z.; Segre, C. U.; Song, C.; Wang, X.; Guo, X. Engineering a Self-Grown TiO2/Ti-MOF Heterojunction with Selectively Anchored High-Density Pt Single-Atomic Cocatalysts for Efficient Visible-Light-Driven Hydrogen Evolution. *Angewandte Chemie International Edition* **2023**, *62*, e202217439.

(60) Navalón, S.; Dhakshinamoorthy, A.; Álvaro, M.; Ferrer, B.; García, H. Metal–Organic Frameworks as Photocatalysts for Solar-Driven Overall Water Splitting. *Chemical Reviews* **2023**, *123*, 445-490.

(61) García-Baldoví, A.; Del Angel, R.; Mouchaham, G.; Liu, S.; Fan, D.; Maurin, G.; Navalón, S.; Serre, C.; Garcia, H. Active site imprinting on Ti oxocluster metal–organic frameworks for photocatalytic hydrogen release from formic acid. *Energy & Environmental Science* **2023**.

(62) Jiao, Y.; Zheng, Y.; Davey, K.; Qiao, S.-Z. Activity origin and catalyst design principles for electrocatalytic hydrogen evolution on heteroatom-doped graphene. *Nature Energy* **2016**, *1*, 16130.

(63) Dronskowski, R.; Blöchl, P. E. Crystal orbital Hamilton populations (COHP): energy-resolved visualization of chemical bonding in solids based on density-functional calculations. *The Journal of Physical Chemistry* **1993**, *97*, 8617-8624.

(64) Jia, G.; Wang, Y.; Cui, X.; Zhang, H.; Zhao, J.; Li, L. H.; Gu, L.; Zhang, Q.; Zheng, L.; Wu, J.; Wu, Q.; Singh, D. J.; Li, W.; Zhang, L.; Zheng, W. Wet-chemistry hydrogen doped TiO2 with switchable defects control for photocatalytic hydrogen evolution. *Matter* **2022**, *5*, 206-218.